Check for updates

ADVANCED MATERIALS
www.advmat.de

Scalable Non-Volatile Tuning of Photonic Computational Memories by Automated Silicon Ion Implantation

*Akhil Varri, Shabnam Taheriniya, Frank Brückerhoff-Plückelmann, Ivonne Bente, Nikolaos Farmakidis, Daniel Bernhardt, Harald Rösner, Maximilian Kruth, Achim Nadzeyka, Torsten Richter, Christopher David Wright, Harish Bhaskaran, Gerhard Wilde, and Wolfram H. P. Pernice**

Photonic integrated circuits (PICs) are revolutionizing the realm of information technology, promising unprecedented speeds and efficiency in data processing and optical communication. However, the nanoscale precision required to fabricate these circuits at scale presents significant challenges, due to the need to maintain consistency across wavelength-selective components, which necessitates individualized adjustments after fabrication. Harnessing spectral alignment by automated silicon ion implantation, in this work scalable and non-volatile photonic computational memories are demonstrated in high-quality resonant devices. Precise spectral trimming of large-scale photonic ensembles from a few picometers to several nanometres is achieved with long-term stability and marginal loss penalty. Based on this approach, spectrally aligned photonic memory and computing systems for general matrix multiplication are demonstrated, enabling wavelength multiplexed integrated architectures at large scales.

1. Introduction

The demands for drastically increasing computing power[1] combined with the imminent end of transistor scaling[2] have been the main drivers for research into alternate computing paradigms. Integrated photonics as a promising platform for neuromorphic computing,[3] mixed-precision accelerators,[4,5] and quantum computing,[6] has garnered heavy attention recently in academia as well as industry.[7–10] The rationale for results from advantages in bandwidth, latency, and power consumption. These factors have successfully led to fiber optics revolutionizing the telecommunications industry. Miniaturized photonic circuits which translate manufacturing advances from the complementary metal-oxide-semiconductor (CMOS) industry to optics have served as a game-changer for implementing optical computing paradigms in a chip-scale setting.[11,12] Similarly, rapid developments in silicon photonics have found applications for networking in data centers[13,14] with the goal of replacing the electrical interconnects in the servers even at shorter distances to meet the ever-increasing demands of big data.

A. Varri, F. Brückerhoff-Plückelmann, I. Bente, W. H. P. Pernice
Institute of Physics
University of Münster
Heisenbergstr. 11, 48149 Münster, Germany
E-mail: wolfram.pernice@kip.uni-heidelberg.de

A. Varri, F. Brückerhoff-Plückelmann, I. Bente, W. H. P. Pernice
Center for Soft Nanoscience
University of Münster
Busso-Peus-Street 10, 48149 Münster, Germany

The ORCID identification number(s) for the author(s) of this article can be found under https://doi.org/10.1002/adma.202310596

© 2023 The Authors. Advanced Materials published by Wiley-VCH GmbH. This is an open access article under the terms of the Creative Commons Attribution-NonCommercial License, which permits use, distribution and reproduction in any medium, provided the original work is properly cited and is not used for commercial purposes.

DOI: 10.1002/adma.202310596

S. Taheriniya, H. Rösner, G. Wilde
Institute of Materials Physics
University of Münster
Wilhelm-Klemm-Street 10, 48149 Münster, Germany

S. Taheriniya, W. H. P. Pernice
Kirchhoff-Institute for Physics
Heidelberg University
Im Neuenheimer Feld 227, 69120 Heidelberg, Germany

N. Farmakidis, H. Bhaskaran
Department of Materials
University of Oxford
Parks Road, OX1 2JD Oxford, UK

D. Bernhardt, A. Nadzeyka, T. Richter
RAITH Nanofabrication
Konrad-Adenauer-Allee 8, 44263 Dortmund, Germany

M. Kruth
Ernst Ruska-Centre for Microscopy and Spectroscopy with Electrons and Peter Grünberg Institute
Forschungszentrum Jülich
52425 Jülich, Germany

C. D. Wright
Department of Engineering
University of Exeter
EX4 4QF Exeter, UK

In addition, PICs have also attracted a lot of attention recently[15–17] due to their ability to integrate with functional materials such as a phase-change material (PCM). PCMs can be used to alter the phase or amplitude of light via evanescent coupling. These properties can be switched either optically or electrically on a sub-nanoscecond timescale and are non-volatile in nature. Hence, their integration with PICs holds significant promise in the push toward optical memories and in-memory computing.

Nevertheless, a key challenge in upscaling integrated photonic systems is the sensitive nature of the components to fabrication imperfections. Since photonic circuits are usually designed to operate in the analog domain, standard process variations in etching rate, exposure parameters, and chemical mechanical polishing conditions adversely affect their functionality.[18–21] For example, a 2% error in the splitting ratio of a beam splitter results in an accuracy degradation of over 50% in a two-hidden layer fully connected feedforward neural network used for performing MNIST handwritten digit recognition.[22] Photonic components that are even more sensitive to fabrication variations are wavelength filters based on interferometers, waveguide gratings, or micro-ring resonators. Such devices are used for implementing wavelength division multiplexing (WDM), a workhorse in data center networks.[23–25] For spectral photonic filters, a 1 nm deviation in the thickness of waveguides can result in wavelength shifts of around 1–2 nm which interfere with several communication channels in a dense WDM network.[26]

The solution to this problem lies in precisely controlling the optical path length or the effective refractive index of individual components to tailor their output and correct for errors post-fabrication. Prominent techniques accomplish this via active phase shifters using thermo-optic heaters, electro-optic modulators (EOM), or micro-electromechanical systems-based devices.[27] In silicon photonics, modulating the free carrier densities in a diode configuration results in a refractive index change.[28] Nevertheless, there are two major drawbacks to active tuning methods: First, a significant part of the power budget is exhausted during operation. Standard CMOS-compatible thermo-optic phase shifters consume around 20 mW for a pi phase shift in a device.[29] Scaling this to a wafer scale containing hundreds of thousands of devices is challenging. The second issue is that additional electronic circuitry is required for operation, thus increasing the complexity and footprint of the circuit design. Furthermore, the thermal and electrical crosstalk is also a concern.

Therefore, passive approaches that manipulate the optical properties in a material are an attractive solution. Such approaches include altering either the waveguide or cladding material post-fabrication to obtain a controlled change in the refractive index. Previous work based on electron beam modification of various cladding materials like silicon dioxide (SiO_2), hydrogen silsesquioxane, and polymethyl methacrylate (PMMA) has shown promise in this regard.[30–32] However, a major challenge with these approaches is that the wavelength shifts obtained are not stable with time. An alternative approach to tuning the optical properties is by amorphizing crystalline silicon waveguides with germanium (Ge) ion implantation.[33,34] Permanent trimming has been observed in this case but requires local annealing for every device via active components such as thermo-optic heaters. Another concern is that Ge absorbs light around 1550 and 1300 nm wavelength ranges,[35] which is the industry standard for fiber optics communications and many other applications. This will induce losses that can be critical, especially for emerging applications in quantum photonics where high-quality factors are desired for performing non-linear operations.

Here, we demonstrate a flexible method for tuning photonic circuits at scale using automated silicon ion implantation in silicon nitride waveguides via marker search and alignment with combined scanning electron microscopy (SEM)-focussed ion beam (FIB) processing, as shown in **Figure 1a**. Silicon nitride (Si_3N_4) is an ultra-low-loss platform and is very well-established in the CMOS industry.[36] We obtain controlled and stable shifts in the optical properties without the need for any active elements. Moreover, being mask-less, our approach does not need to be performed at the end of the process flow since there is no need to use a specific cladding material. After performing the tuning operation, further fabrication processes such as the deposition of PCMs or electrodes do not affect the circuit. We carried out a detailed material study using scanning transmission electron microscope (STEM) energy-dispersive spectroscopy (EDS) and electron energy loss spectroscopy (EELS) analysis to understand the fundamental changes occurring at the atomic scale. Leveraging these advances, for the first time, we demonstrate passively aligned energy-efficient photonic circuits enabling applications in wavelength addressable memory and a photonic computing engine exploiting WDM.

2. Results and Discussions

2.1. Photonic Device Tuning

As wavelength selective on-chip components, we use photonic micro-ring resonators. Ring resonators are widely employed in photonic communication systems, sensing, quantum technologies, and optical computing applications.[37] What makes them interesting for showcasing our approach is their sensitivity to fabrication imperfections and environmental conditions. Even slight variations in the geometry of the ring lead to significant shifts in resonance, which can be detrimental to the operation of a given circuit where multiple resonators must be aligned with respect to each other. Whenever the round-trip phase accumulated inside a ring, given by $2\pi n_{\text{eff}} L/\lambda$, equals multiples of 2π, the resonant condition occurs. Here n_{eff} is the effective refractive index which depends on the geometry of the waveguide and material properties, and L is the total path length of the ring. Altering the optical path length of the ring translates to shifts in resonances. In our case, the change in optical path length is achieved by creating silicon-implanted regions of increasing length which leads to redshifts in the transmission spectrum as shown schematically in Figure 1b. The implantation is carried out using targeted FIB irradiation at a specific position on the ring, aligned with respect to marker structures fabricated in the vicinity of the resonator. By controlling the length of the implanted region, a desired spectral shift is achieved.

2.2. Characterizing the Material Changes

We fabricate Si_3N_4 photonic devices with the approach described in the Experimental Section. During FIB implantation of silicon

© 2023 The Authors. Advanced Materials published by Wiley-VCH GmbH
15214095, 2024, 8, Downloaded from https://onlinelibrary.wiley.com/doi/10.1002/adma.202310596 by University Of Exeter, Wiley Online Library on [19/06/2024]. See the Terms and Conditions (https://onlinelibrary.wiley.com/terms-and-conditions) on Wiley Online Library for rules of use; OA articles are governed by the applicable Creative Commons License

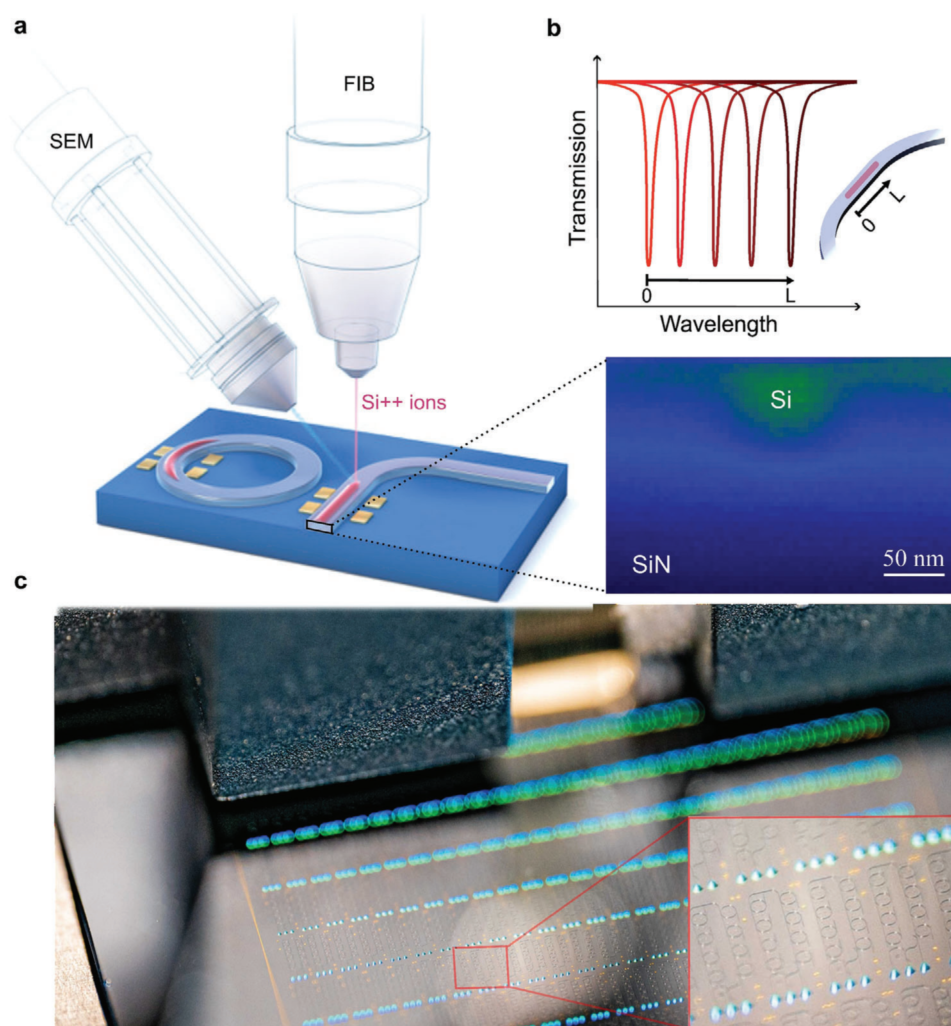

Figure 1. Photonic device tuning by automatized silicon implantation. a) Silicon ion patterning on photonic circuits using the Raith VELION focused ion beam. The photonic circuits consist of silicon nitride ring resonators on top of the SiO_2 substrate. The ions are directly written into the waveguide without requiring a mask. The inset on the right displays the plasmon map reconstructed from low loss energy spectrum. The patterning process leads to silicon ion implantation in the Si_3N_4 waveguides. b) Schematic of the optical response. Redshifts in the transmission spectrum of ring resonators with larger pattern lengths confirm the increase in the effective refractive index of the waveguide material. c) A photograph of the integrated photonic chip showing the scale of the approach. The inset shows a few photonic circuits and gold markers that are used for automatic patterning in the FIB.

from liquid metal alloy ion sources (LMAIS), a local silicon-rich region is created within the waveguide. This is illustrated schematically in the inset of Figure 1a. In order to characterize the devices after tuning, we perform a step-by-step analysis of microstructural aspects that are influenced by the implantation process. Upon close examination of the surface morphology in **Figure 2a** the SEM image acquired reveals a discernible line atop the waveguide. Notably, the edges and the core of the line exhibit enhanced brightness in the SEM micrograph, suggesting the presence of silicon or the formation of sharper edges which are favorable sites for the accumulation of electrons.

The subsequent atomic force microscope (AFM) analysis of the surface topography in Figure 2b presents evidence that the introduction of Si ions has generated a 15 nm high bump on the surface flanked by distinctively sharper edges on either side. The surface profile is due to a combination of the implantation and sputtering processes that occur simultaneously during FIB processing. In our case, the sputter yield of the target silicon nitride material is very low with a Si ion beam, and the whole process is dominated by the former. The bump shown in the AFM analysis can be attributed to the implantation process which induces stress in the material due to the displacement of atoms. This has been previously shown in amorphous metal ribbons to result in a local free volume expansion.[38] Additionally, the sputter process results in the target silicon nitride material getting redeposited on sides of the ion beam path. This is a common phenomenon during ion beam sputtering/milling.[39] We expect the sharp edges on either side of the bump to be the gaps between the central bump and redeposited material at the sides.

Figure 2c shows the STEM EDS elemental mapping of the Si_3N_4 waveguides subjected to patterning. The results indicate a distinguishable and localized increase in the atomic fraction of

© 2023 The Authors. Advanced Materials published by Wiley-VCH GmbH

15214095, 2024, 8, Downloaded from https://onlinelibrary.wiley.com/doi/10.1002/adma.202310596 by University Of Exeter, Wiley Online Library on [19/06/2024]. See the Terms and Conditions (https://onlinelibrary.wiley.com/terms-and-conditions) on Wiley Online Library for rules of use; OA articles are governed by the applicable Creative Commons License

15214095, 2024, 8, Downloaded from https://onlinelibrary.wiley.com/doi/10.1002/adma.202310596 by University Of Exeter, Wiley Online Library on [19/06/2024]. See the Terms and Conditions (https://onlinelibrary.wiley.com/terms-and-conditions) on Wiley Online Library for rules of use; OA articles are governed by the applicable Creative Commons License

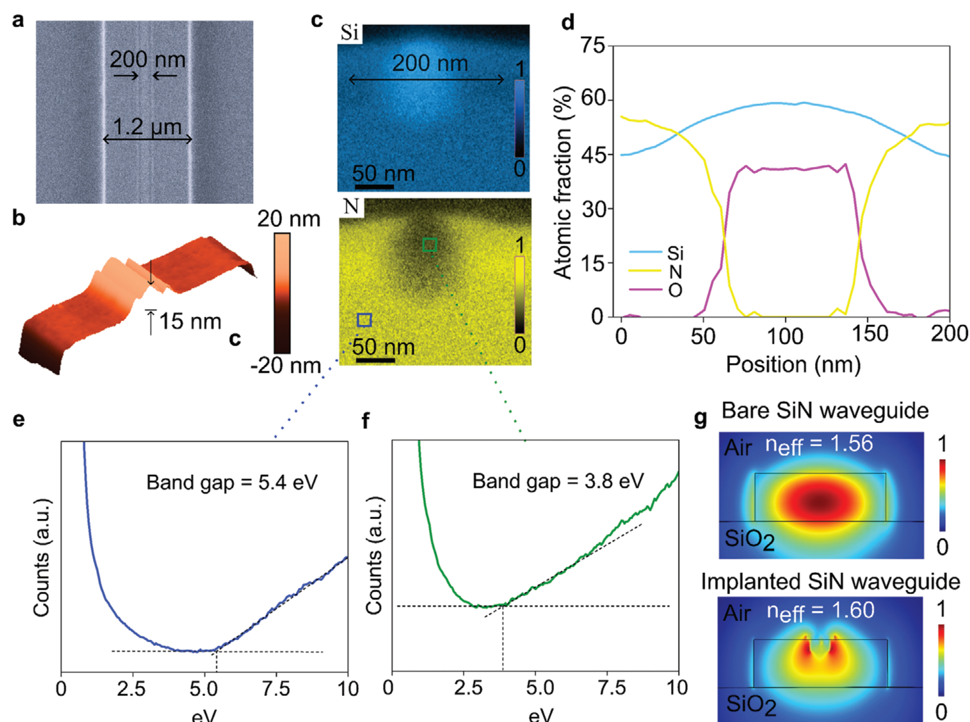

Figure 2. Material and microstructural analysis: a) High-resolution SEM micrograph depicting the intricate surface morphology of the Si_3N_4 waveguide after Si implantation. b) 3D AFM visualization, showcasing the topographic details and revealing a prominent 15 nm elevated protrusion that induces lateral displacement of the Si_3N_4 material, thereby introducing additional surface roughness in the vicinity of the Si implantation site. c) STEM EDS elemental maps, employing a color scale representation, highlighting localized increase in the atomic fraction of Si and suggestive of potential intermixing due to perturbation in the chemical composition of the pristine material. d) EELS line scans derived from the high-loss signal, providing precise spatial distribution information regarding the constituent elements in the implanted region. It exhibits a discernible presence of silicon and oxygen. e) Bandgap of the non-implanted waveguide region obtained from EELS plasmon maps. f) Bandgaps of the implanted region. g) Simulated fundamental transverse-electric (TE) mode profiles propagating inside the waveguide for bare and implanted configuration showing the contrast in electric-field distribution and effective index.

Si. This presents a high potential for the disruption of existing bonds and the formation of new bonds between the constituent elements of the host material and the implanted Si ions. The implantation profile we observe here also closely matches the ion trajectory simulations (shown in Section S1, Supporting Information).

Figure 2d displays the same region, which underwent additional investigation using the EELS elemental mapping. The line scan at the center of implanted region exhibits an increase in Si concentration to 60% and shows a notable presence of oxygen which increases up to 40%. The findings of the EDS analysis are confirmed by this independent technique with complementary information on the local concentration of lighter elements such as nitrogen and oxygen.

The EELS investigation was additionally employed to discern the alterations in the optical characteristics of the Si_3N_4 waveguide, as elucidated by the plasmon map in Figure 1a. The corresponding bandgap estimations for the pristine waveguide region and the Si implanted region are shown in Figure 2e,f, respectively. An expected decrease in bandgap is observed in the implanted region shifting the absorption edge to higher wavelength of incident photons. The integration of data points acquired from EELS elemental mapping and plasmon mapping facilitated the estimation of the spatial distribution and evolution of the refractive index. This was achieved by constructing a refractive index matrix that captures the intricate distribution and dynamic evolution of the refractive index, arising from the Si ion implantation and localized intermixing of Si_3N_4 with Si ions.

We employ this data to perform finite element method simulations to estimate the impact of our process on the optical properties at 1550 nm wavelength for a 330 nm high and 1.2 µm wide Si_3N_4 waveguide. Figure 2g shows that the implantation increases the mode confinement of the fundamental mode, pulling the fields around the implanted region, which results in an increase in the n_{eff}. The change in the mode profile for the implanted configuration also results in different dispersion characteristics (see Figure S12, Supporting Information). The results suggest that optimizing the implantation patterning parameters can be an interesting tool for dispersion engineering. Finally, we use the obtained n_{eff} value to analytically calculate the expected resonance shift. This closely matches the measurement results, validating our characterization technique. The detailed analytical calculation for the resonance shifts is provided in the Experimental Section. Based on this analysis, we can locally tune the optical properties of the waveguide to a desired spectral position after fabrication.

© 2023 The Authors. Advanced Materials published by Wiley-VCH GmbH

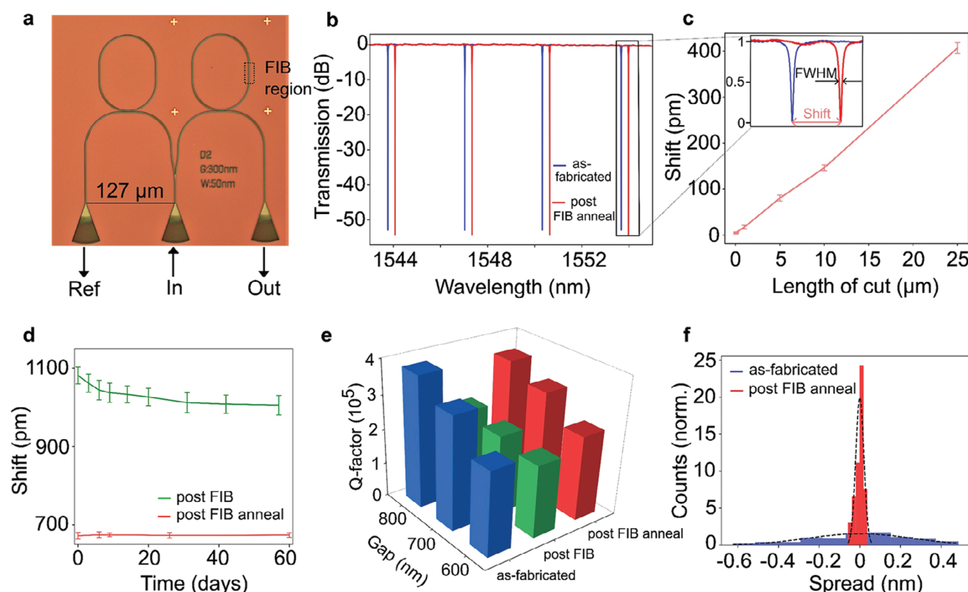

Figure 3. Spectral alignment through silicon implantation. a) Optical micrograph of the device under test used for calibration. The input is split 50/50 to the reference resonator (left) and implanted resonator (right). The gold crosses around the right ring are used for marker detection in the FIB. b) Transmission spectra before (blue) and after (red) the implantation process. c) Shifts in resonant wavelengths versus different pattern lengths. Other parameters such as the dose (0.1 nC μm^{-2}) and widths (50 nm) are constant. A total of 10 devices per pattern length is used for the tests. d) Stability of shifts. Annealing the sample after the implantation process stabilizes the shifts and also improves the standard deviation as shown in the red curve. e) Study of losses induced due to implantation. All the devices are patterned with the same parameters. The quality factors are retained after annealing even for larger gaps. f) Statistics of the implantation process. The resonance spread of 100 rings spanning the length of our chip is shown before (blue) and after (red) tuning. The area under the histogram is normalized to 1 for both cases.

2.3. Optical Response of the Implantation Process

Having qualitatively analyzed the material dynamics, we quantitatively assess the process by optical measurements. An exemplary test device with two race-track resonators is shown in **Figure 3a**. The reference ring on the left is used to calibrate the effects of measurement and environmental conditions. We pattern a straight section of the racetrack to standardize the effect of implantation with respect to the length of the pattern. The redshift observed in the transmission spectra due to silicon ion implantation can be clearly seen in Figure 3b. The inset of this figure plots the spectra in absolute units showing the full-width half maximum (FWHM) which is used to estimate the quality factor (Q) of the rings.

Figure 3c shows the deterministic relationship between the shift in resonances and the pattern length of the implanted region. While keeping the dose of the ion beam constant, a linear relationship between the length of the pattern and shift is obtained. Here, a shift ranging from 6 ± 1 pm to 400 ± 10 pm is observed for lengths ranging from 100 nm to 25 μm. Larger shifts in the nm range can also be produced by using higher doses or larger widths (shown in Section S2, Supporting Information). The stability of the induced shifts with time under ambient environmental conditions is shown in Figure 3d. After patterning, as depicted in the green curve, the shift starts to decay with time because the implantation process creates defects and impurities which are prone to chemical reactions in the atmosphere. This was confirmed with EELS elemental maps, where the post-FIB sample was heavily contaminated. However, annealing the sample in a tube furnace after FIB writing aids in thermal diffusion and removes the ion-induced damage. The heat treatment not only facilitates the relaxation of Si_3N_4 following Si implantation, but also engenders an additional oxidation process within the confines of the tube furnace (more details in Table S1, Supporting Information).

This oxidative transformation effectively lowers the surface energy by the formation of new chemical bonds, thereby contributing to the enhanced stability and robustness of the material. We observe a blue shift immediately after annealing as shown in the red curve which remains constant afterward. The stability tests were performed by leaving the chip in ambient conditions with exposure to different temperatures, air pressure, humidity, and the presence of dust particles. The shifts obtained also show stability after performing further lithography and deposition steps. We also found that further annealing steps on the same chip do not impact the stability of the already-tuned devices. This characteristic is especially crucial in making the implanted devices compatible within a packaged circuit that could be subject to elevated operational temperatures due to neighboring electronics.

Next, we analyze the optical loss induced during the implantation process by comparing Q-factors before and after tuning. The Q-factor is inversely proportional to the power loss per round trip. High Qs in the order of 10^5 and 10^6 are desired for obtaining strong non-linear interactions for applications such as generating entangled photons. By increasing the gap between the bus waveguide (used for probing light in and out) and the ring, the ring resonator can be moved from an over-coupling to an under-coupling regime. This increases the lifetime of a photon inside the ring and results in high Qs (more details are presented in Section S2, Supporting Information). In Figure 3e, the change

© 2023 The Authors. Advanced Materials published by Wiley-VCH GmbH

15214095, 2024, 8, Downloaded from https://onlinelibrary.wiley.com/doi/10.1002/adma.202310596 by University Of Exeter, Wiley Online Library on [19/06/2024]. See the Terms and Conditions (https://onlinelibrary.wiley.com/terms-and-conditions) on Wiley Online Library for rules of use; OA articles are governed by the applicable Creative Commons License

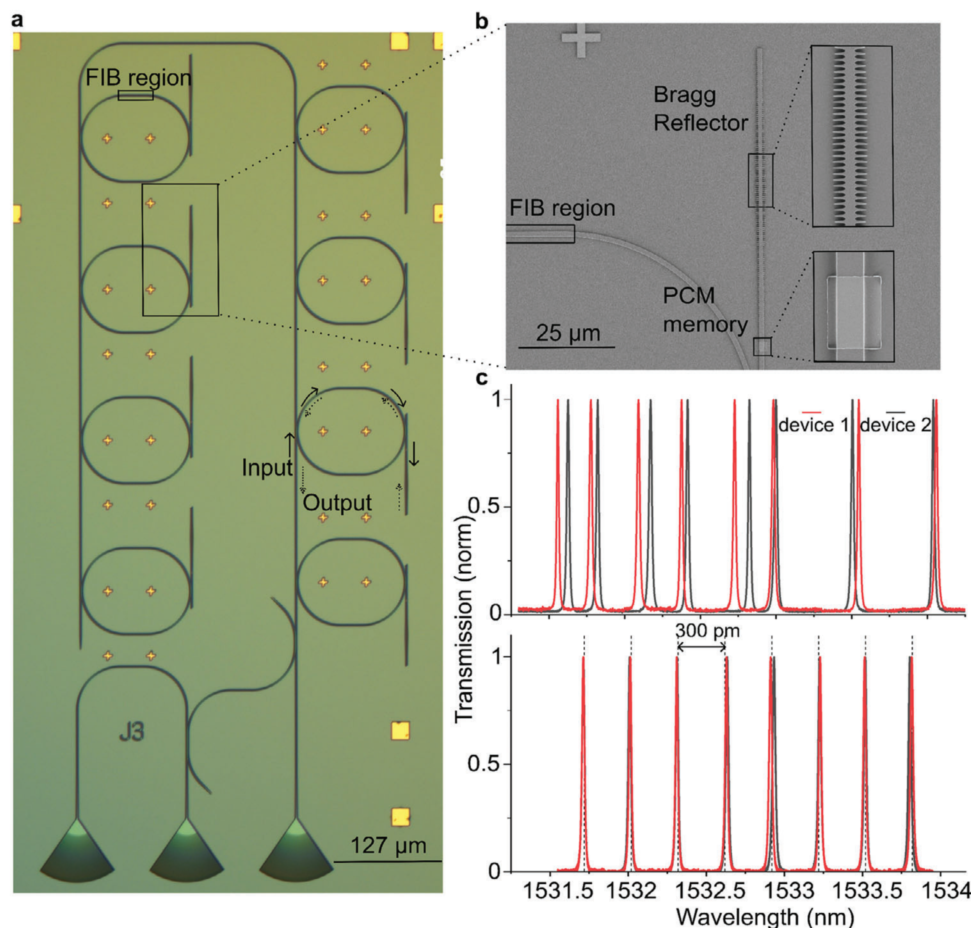

Figure 4. Wavelength addressable photonic memory. a) Optical micrograph of one memory block that can store up to 8 analog values. The combination of a ring, PCM memory, and Bragg filter acts as a unit cell. The solid and dotted arrows trace the path of the light for one unit cell showing the input and output respectively. b) Mechanism of memory storage in a unit cell. Light couples from the ring to the adjacent waveguide where it interacts with a PCM cell that modulates its intensity. After this interaction, the light gets reflected using a Bragg grating, interacts again with the PCM cell, and couples back into the ring for the readout. c) Transmission spectrum of two devices after device fabrication (upper panel) and post-FIB tuning (lower panel).

Table 1. Extracted propagation losses in the waveguide.

As-fabricated [dB cm^{-1}]	Post FIB [dB cm^{-1}]	Post FIB anneal [dB cm^{-1}]
0.88	1.43	0.95

in the Q-factor due to the implantation process is shown. As the Q value of the intrinsic resonator gets higher, patterning with the same dose and size leads to a larger loss. Nevertheless, annealing the sample post-FIB recovers the Q values to around half a million. This result is also consistent with the findings concerning annealing described above.

By extrapolating the measured Q values to the weakly-coupled case, the propagation losses are determined and shown in **Table 1**. The loss values are given for a dose of 0.1 nC μm^{-2} which is used for obtaining the shifts in Figure 3. These values can be further reduced by decreasing the dose which will reduce the reflections at the interface between fabricated and implanted regions, assumed to be the main contribution to the loss induced through our process. Furthermore, patterning the entire racetrack or introducing a taper before and after the implanted section can also minimize the losses enabling adiabatic mode transition. With a reduced dose, higher shifts can still be obtained by increasing the length of the pattern.

To analyze the reproducibility of our approach, Figure 3f depicts statistics collected from ring resonator tuning. The blue histogram shows the resonance spread after fabrication for 100 rings identical in design. The red curve shows the spread in resonances for identical FIB patterns designed to perform a coarse tuning operation. Here, the standard deviation of the target resonance for 100 rings is reduced to 20 pm. In order to achieve even higher precision, coarse tuning can be followed up with a fine-tuning operation which as shown in Figure 3b can be used to achieve sub-10 pm accuracy. This is employed in the applications described in the following section.

2.4. Wavelength-Addressable Optical Memory

As a first example, we demonstrate an optical memory architecture shown in **Figure 4a** using multiple add-drop ring resonators

© 2023 The Authors. Advanced Materials published by Wiley-VCH GmbH

15214095, 2024, 8, Downloaded from https://onlinelibrary.wiley.com/doi/10.1002/adma.202310596 by University Of Exeter, Wiley Online Library on [19/06/2024]. See the Terms and Conditions (https://onlinelibrary.wiley.com/terms-and-conditions) on Wiley Online Library for rules of use; OA articles are governed by the applicable Creative Commons License

combined with functional materials. Here, we store information in the light's amplitude that is modulated through evanescent interaction with PCM. We use the ternary alloy $Ge_2Sb_2Te_5$ (GST) well-known for its non-volatile memory functionality. For GST, a change in the structure from amorphous to crystalline state leads to an increase in the absorption coefficient which is exploited for realizing a multi-level memory.[15,40] This functionality has also been used to store matrix weights and perform energy-efficient optical in-memory computing.[12,16]

Our device architecture consists of 8 unit cells, each functioning as a photonic memory which is addressed with a unique wavelength. Within one unit cell, a ring resonator is used to filter specific wavelengths of light. The resonator is connected to a PCM cell that stores information and a Bragg filter which is designed to reflect the incoming light to achieve higher memory depth in a double pass (Figure 4b). This architecture results in a very compact design where the input and output light travels in opposite directions, as shown by the dotted lines (Figure 4a). Each ring is designed to operate at separate wavelengths so that all the rings can be accessed simultaneously. The design details of the Bragg filter and memory architecture are given in Section S3, Supporting Information.

For practical purposes, it is crucial that multiple memory blocks show the same resonance spectra. Otherwise, addressing each device would require 8 unique wavelengths for a fast parallel operation making scalable operation very challenging. Moreover, the scalability could be further improved by designing the resonances equidistant so that a single-frequency comb source can be used for read and write access.[41] In the upper panel of Figure 4c, we show the transmission spectra of two memory blocks that were designed to have the same equidistant resonances. Before the tuning operation, the spectra are not aligned and show wavelength offsets. Using our implantation process, we correct for the deviations and align the spectra to be equidistant with 300 pm spacing, as shown in the lower panel.

2.5. Photonic Computing for Accelerated General Matrix Multiplications

As a second example, we explore a photonic computing architecture using ring resonators for WDM. Modern data centers employ electronic hardware like graphical processing units and tensor processing units for performing arithmetic tasks such as neural network inferencing. Most of their processing time is spent performing mathematical operations in parallel, that is, matrix-vector multiplications.[42] This has led to a lot of interest in the community to develop specialized matrix multiplication hardware for accelerating artificial intelligence (AI) workloads.[43,44] Photonic solutions have shown great promise lately[12,45] and may complement conventional products in many AI applications. Ring resonator-based configurations are particularly attractive[46–48] since they show non-linear behavior and can be used as multiplexers or demultiplexers inside the circuit allowing for a compact, loss-less, and parallel operation on several wavelengths. However, still plagued by the uncertainties induced due to fabrication, all photonic computing implementations until now have relied on active methods to perform the correction.

Here, we employ a photonic circuit comprising passively tuned ring resonators to carry out matrix-vector multiplications in parallel (**Figure 5a**). We perform convolution operations as used in computer vision for edge detection within an input image. The input image data is encoded in the amplitude of the incoming light. This is done using an EOM for each channel in the matrix. The EOMs are controlled using an external field programmable gate array (FPGA) that sends the input image pixel data at a 2 GHz clock frequency. Once the pixel information is encoded in the input light intensities, they are passed on to the matrix for the multiplication and accumulation operation. We operate in a weight-stationary inference scheme where the kernels are flattened and loaded in the state of the PCM (GST cell). At the output of each column, the convolved image data is obtained for that individual kernel.

Using ring resonators in this photonic circuit allows us to encode the four elements of the input vector in separate wavelengths with none of the rows interacting with one other. This results in negligible additional loss while scaling the rows of the matrix. However, a key requirement is that all three rings in each row need to have the same wavelength for accessing the three kernels simultaneously. This is not the case after fabrication as shown in the upper panel of Figure 5b. Each row in our case is misaligned by around 100–400 pm. These errors are measured and corrected automatically in the FIB using the calibration data. The result is shown in the lower panel of Figure 5b, where all the resonances are perfectly aligned. After the tuning operation, we carry out the PCM deposition. The PCM cells are switched optically to store the flattened kernel data. The optical micrograph and SEM pictures of the fabricated circuit are shown in Section S3, Supporting Information.

Finally, the convolved output is measured using photodetectors at the end of each column. The obtained currents are sent back to the FPGA where the output image is reconstructed. Figure 5c shows the output of three kernels convolved on the test zebra image shown in (i). A blurred output (obtained by using a kernel to implement photonic low-pass filtering) is shown in (ii), whereas (iii) and (iv) show the results of implementing photonic edge-detection in the horizontal and vertical directions respectively.

3. Conclusions

We have demonstrated a scalable, robust, and low loss method for precisely controlling the optical path lengths in silicon nitride photonic integrated circuit devices. The method can be used to effectively correct the random inaccuracies that occur during fabrication in an automated process. We also demonstrated the ability for precise spectral alignment of resonances (e.g., to a microcomb source), and implemented such a system in a passive ring-resonator-based photonic matrix multiplication circuit. If we assume the fabrication error in the resonance wavelength to be 30% of the free spectral range (FSR) (a value based on our measured statistics), and 20 mW power required to tune over the whole FSR (for a conventional thermo-optic phase shifter[29]), we save around 6.66 mW per each resonator compared to an active approach. For our proof of principle matrix multiplication circuit, this accounts to be ≈60 mW reduction in the power budget. For commercial applications that aim for larger matrix sizes such as

© 2023 The Authors. Advanced Materials published by Wiley-VCH GmbH

15214095, 2024, 8, Downloaded from https://onlinelibrary.wiley.com/doi/10.1002/adma.202310596 by University Of Exeter, Wiley Online Library on [19/06/2024]. See the Terms and Conditions (https://onlinelibrary.wiley.com/terms-and-conditions) on Wiley Online Library for rules of use; OA articles are governed by the applicable Creative Commons License

15214095, 2024, 8, Downloaded from https://onlinelibrary.wiley.com/doi/10.1002/adma.202310596 by University Of Exeter, Wiley Online Library on [19/06/2024]. See the Terms and Conditions (https://onlinelibrary.wiley.com/terms-and-conditions) on Wiley Online Library for rules of use; OA articles are governed by the applicable Creative Commons License

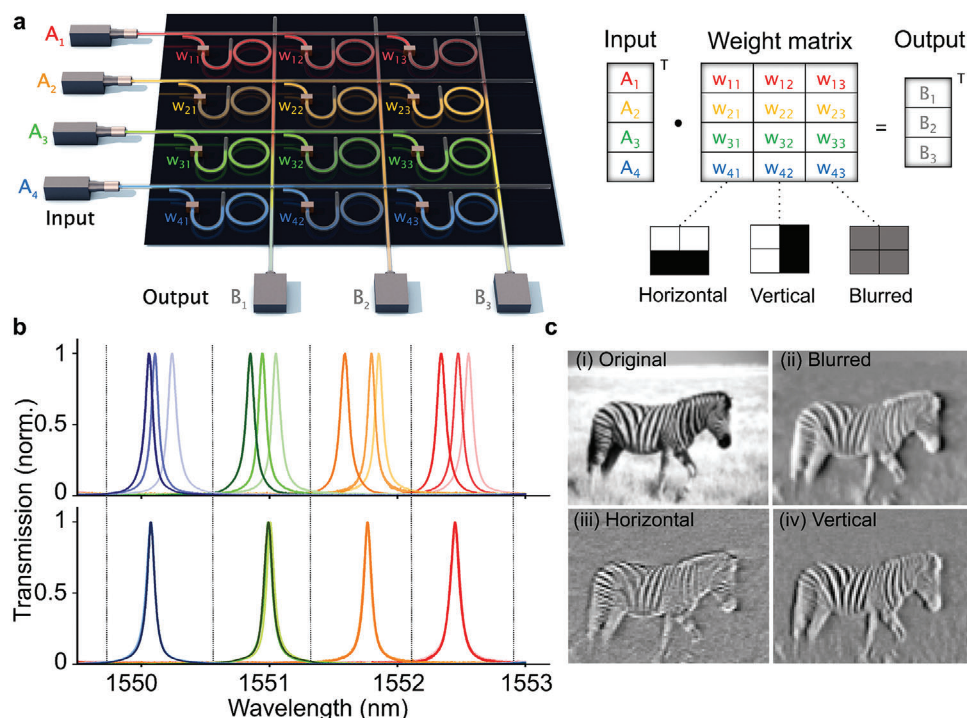

Figure 5. Matrix vector multiplication architecture for edge detection. a) Schematic of a 4 × 3 matrix multiplication circuit. An input image vector that needs to be inferred is encoded in the amplitude of incoming light to the matrix. Each element of the vector is encoded in a unique wavelength for parallel processing. Directional couplers are used to split equal intensities of light from the rows to the PCM cells that store the weights of the network. Ring resonators are used to finally couple the light into the columns. For the ideal configuration, the three resonators in each row are designed to be aligned at the same wavelengths as illustrated inside the color coding of the schematic. b) Transmission spectrum of the circuit right after fabrication (upper panel); and after post-fabrication tuning (lower panel). c) Edge detection example. The grayscale zebra image shown in (i) is sent as the input; (ii), (iii), and (iv) show the output computed for respective filters.

128 × 128, the power budget savings quickly scale to upward of 100 W, a very important and significant improvement in energy efficiency. Similar parallels can be drawn for optical I/O technologies in which a high bandwidth transceiver module can contain up to 8 ring modulators whose transmission spectrum needs to fit WDM schemes. We can readily obtain such spectrums using our implantation method, as we showed in the photonic memory application.

The fact that our process is maskless also allows for further fabrication steps after tuning. We also demonstrated that our approach is robust to temperature and environmental changes. We show that the losses induced due to the ion implantation process are negligible, with high Qs of around half a million. This is crucial for some applications such as photonic quantum computers that demand ultralow losses. We demonstrated the capabilities of our tuning approach via modification of transmission spectra in ring resonator devices, but our process is applicable to other key integrated photonic components such as beam splitters, interferometers, or directional couplers. Indeed, since all of these components are less sensitive than a ring resonator to changes in effective index, our approach will be very well suited to the correction of fabrication tolerances in them. Finally, we point out that our scheme of changing the optical properties using a silicon ion FIB is not just limited to silicon nitride waveguides and could also be translated to other integrated photonics material platforms such as silicon-on-insulator or lithium-niobate-in-insulator.

4. Experimental Section

Device Fabrication: The photonic circuits used in this study were designed using gdshelpers,[49] a Python-based open-source design framework for integrated circuits. The material stack used was stoichiometric low pressure chemical vapor deposited (LPCVD) Si_3N_4 films (330 nm) on top of SiO_2 dielectric (3300 nm) with silicon as the substrate material. The cladding on top was air. The wafers were acquired from Rogue Valley Microdevices. The process flow consists of three steps, first was to write the gold markers required for later steps. In the second step, the photonics was patterned. The PCM (GST) patterning was done at last.

For the gold markers, the process started with spin-coating the positive photoresist PMMA from AllResist AR-P 672 series. After baking the resist, a 100 kV electron beam lithography tool (Raith EBPG 5150) was used to expose the marker regions. Next, the chip was developed in a methyl isobutyl ketone (MIBK) and isopropyl alcohol (IPA) solution. Following this, a stack of chromium (5 nm)/gold (80 nm thick)/chromium (5 nm) was deposited on the chip using physical vapor deposition (PVD). The chromium on the bottom and top was used for better adhesion and protection of the gold surface. Last, the liftoff process of the resist was undergone in acetone to get the final markers. For the next two steps, these markers were used for alignment.

Photonics was written using a negative resist (AR-N 7520 series) that was spin-coated for obtaining a thickness of 350 nm.

© 2023 The Authors. Advanced Materials published by Wiley-VCH GmbH

The waveguide regions were then exposed using the electron beam with small currents and step sizes to obtain high accuracy. After developing this chip in the Microposit MF-319 solution, the mask ready was ready for etching. This was done using a reactive ion etching tool from Oxford Instruments. A plasma consisting of CHF3 and O2 was used to etch the un-exposed silicon nitride regions. The last step was to strip the resist using oxygen plasma.

For patterning GST, the same steps as those for gold were followed. The PMMA resist was exposed in regions where the PCM was desired. After development, 10 nm GST was sputtered on top of the chip, followed by the sputtering of a 10 nm layer of ITO as a protective layer on top. Finally, acetone was used to liftoff the resist.

Post-Fabrication Tuning: The Raith VELION FIB,[50] capable of providing various ion species from LMAIS, was used to tune the refractive index of silicon nitride waveguides. A 35 kV Si++ beam with an aperture size of 30 μm was selected for the implantation process. The patterns that need to be written using the FIB were set on a separate layer in a GDSII design file, which was the industry standard for IC layout. This file was loaded into the FIB and patterning was carried out using marker alignment in a maskless process. Post-FIB, the samples were annealed in a tube furnace at 400 °C for 2 h to stabilize the shifts.

For tuning the photonic circuits, the fabrication deviations were measured in an automatic measurement setup. The shifts required for aligning everything were then mapped to the length of the FIB pattern using calibration data (similar to Figure 3c). Finally, this design was loaded into the FIB, and the rings were aligned in a fully automated process.

Microscopy and Sample Preparation: The Si_3N_4 waveguides were further analyzed in the as-fabricated and implanted states using a TEM. Prior to the TEM microscopy, thin lamellae were prepared from the regions of interest using the FIB technique in a ZEISS Crossbeam 340 SEM/FIB. Thereafter, these prepared thin samples were studied using a Titan Themis G3 300 TEM (FEI) microscope operated in STEM mode. Elemental mapping was performed using EDS with a quadrupole EDX system, and a high-angle annular dark-field (HAADF) detector (Fischione Model 3000). The high brightness field emission gun (X-FEG) in this microscope was operated at 3.45 kV extraction voltage and 300 kV acceleration voltage, along with a monochromator. EELS was performed in STEM mode at 60 kV in the form of spectrum imaging using a Quantum 965 ER Gatan imaging filter (GIF). The following experimental parameters were used: a probe size of 0.5 nm, a beam current of 36 pA, an energy resolution of 0.5 eV, an energy dispersion of 0.05 eV channel^{-1}, a convergence semi-angle of 22 mrad, and a collection semi-angle of 10 mrad acquiring EELS spectra with 40 ms dwell-time subsequently integrating over 5 frames.

Numerical Analysis and Simulations: The mode profiles were simulated using Lumerical Mode, a Finite-Difference Eigenmode solver. The silicon implantation region was modeled by a map of coefficients that contained the composition of Si_3N_4 and Si for each pixel. This coefficient map was acquired from EELS elemental mapping and plasmon mapping. The wavelength-dependent refractive indices of the implanted region were finally obtained by taking a weighted sum of these coefficients. The material dispersion data for Si and Si_3N_4 used in these calculations was fitted to the Selmeier equation.[51,52] For the mesh settings, a combination of graded and conformal meshing available in Lumerical was used. The implanted region had a finer mesh with a maximum mesh size of 10 nm. The simulation region was large enough such that the evanescent fields decayed completely leading to minimal reflections. Metal boundary conditions were used for the simulation region.

After solving Maxwell's equations on a cross-sectional mesh of the waveguide, the solver returns the mode profile and effective index of the fundamental TE mode. Plugging in the effective index into the formulae $2\pi n_{\text{eff}} L = m\lambda$, the shift in wavelength can be calculated. In the formula above, $n_{\text{eff}} L$ is a combination of the implanted straight section and the rest as-fabricated racetrack. For the case shown in Figure 2 of the main text, the calculated shift was 2.7 nm for a 50 μm ring radius and two 25 μm straight sections (one of which was implanted with 200 nm pattern width and 0.8 nC μm^{-2} dose). This was in concurrence with the experimental data shown in Figure S11, Supporting Information, where shifts up to 2 nm can be observed for a similar patterning width.

The simulation of the Bragg cavities was performed using Lumerical's variational finite-difference time-domain solver. The fundamental TE mode source was injected through the input, and the transmission, reflection, and electric-field propagation along the cavity were studied.

Measurement Setup: For the optical characterization experiments shown in Figure 3, a simple scheme consisting of a tunable laser source (Santec TSL-710), a polarization controller, a fiber array, and a photodetector (Newport Model 2011) was used. The chip was placed on top of a vacuum-enabled stage that can be controlled through piezo motors via a closed-loop algorithm enabling sub-micron precision. Using this, the measurement process was automated in such a way that the stage moved under the fiber array to the next region of interest, optimized the transmission, performed a wavelength sweep, and saved the data. A schematic of this setup is shown in Section S2, Supporting Information.

Here, light was coupled in and out of the chip using grating couplers. For calculating the shifts, the difference between the output resonance positions and reference resonance positions before and after patterning (Figure 3a) was studied. In this way, the effect of environmental and measurement conditions was negated. In the memory application shown in Figure 4, a commercially available gas reference cell (HCN) was used for precisely calibrating the wavelengths.

In the convolution measurement (Figure 5), a CW laser source was used as input for each row. Each laser emits light at a unique wavelength specific to its input row. Next, the light was intensity-modulated using analog EOMs from Optilab whose 3 dB bandwidth was 30 GHz. Using this, pulses were generated, with each pulse encoding a pixel value from the input. The EOMs were controlled electrically using an FPGA, which stores the input image digitally. This image was fragmented according to the kernel size, passed on to a digital-to-analog converter (DAC) and sent to the EOM for encoding the data in light intensities. This light was coupled into the chip using a fiber array and grating couplers, similar to the setup mentioned earlier. The matrix multiply and accumulate operations for all three kernels take place parallelly on-chip at the speed of light. The output for each kernel was measured at the end using photodetectors from Thorlabs that can go up to

© 2023 The Authors. Advanced Materials published by Wiley-VCH GmbH
15214095, 2024, 8, Downloaded from https://onlinelibrary.wiley.com/doi/10.1002/adma.202310596 by University Of Exeter, Wiley Online Library on [19/06/2024]. See the Terms and Conditions (https://onlinelibrary.wiley.com/terms-and-conditions) on Wiley Online Library for rules of use; OA articles are governed by the applicable Creative Commons License

ADVANCED MATERIALS
www.advmat.de

10 GHz. The detected photocurrents were sent to the analog to digital converters (ADCs) on the FPGA and the convoluted images were reconstructed. The entire convolution operation was performed at a fast clock rate of 2 GHz, limited only by electronic components such as DACs and ADCs. A schematic of the setup is shown in Section S3, Supporting Information.

Statistical Analysis: The bandgap data in Figure 2e,f were obtained by taking the intersection from the horizontal background level and the curve obtained by linear fitting the low loss spectrum. This was performed in the DigitalMicrograph software from Gatan. The error bars in Figure 3c,d indicate the standard deviation for each parameter. A total of 10 devices per pattern length were used in Figure 3c. The stability test (Figure 3d) was shown for 20 devices that were patterned with the same length and dose. There were no outliers in the data. The Q-factor data in Figure 3e were obtained by fitting each transmission spectra to a perfect Lorentzian fit (R-squared of 100%). The histogram data in Figure 3f were normalized such that the area under the histogram was 1 for both the as-fabricated and post-FIB annealed cases. The total number of samples for the histogram data was 100. These devices span the entire length of the 15 mm chip. The transmission spectra shown in Figures 4c and 5b were normalized to one.

Supporting Information

Supporting Information is available from the Wiley Online Library or from the author.

Acknowledgements

F.B.-P. and W.H.P.P. acknowledge support from the Volkswagen Foundation. W.H.P.P. acknowledges the support of the European Research Council (ERC, PINQS project). The authors thank Jochen Stuhrmann for assistance with the graphical illustrations and Jonas Schütte with the optical images. This work was supported by the European Union's Horizon 2020 research and innovation programme (grant no. 101017237, PHOENICS project) and the European Union's Innovation Council Pathfinder programme (grant no. 101046878, HYBRAIN project). The authors acknowledge funding support by the Deutsche Forschungsgemeinschaft (DFG, German Research Foundation) under Germany´s Excellence Strategy EXC 2181/1—390900948 (the Heidelberg STRUCTURES Excellence Cluster), the Excellence Cluster 3D Matter Made to Order (EXC-2082/1—390761711) and CRC 1459 "Intelligent matter."

Open access funding enabled and organized by Projekt DEAL.

Conflict of Interest

The authors declare no conflict of interest.

Author Contributions

A.V., S.T., and F.B.P. performed the experiments with assistance from I.B. and D.B. S.T. and H.R. performed the TEM analysis. M.K. assisted in the TEM sample preparation. A.V. and D.B. performed the Si implantation with assistance from A.N. and T.R. All authors analyzed the data and wrote the manuscript.

Data Availability Statement

The data that support the findings of this study are available from the corresponding author upon reasonable request.

Keywords

electron energy-loss spectroscopy, focused ion implantation, micro-ring resonators, photonic integrated circuits, wavelength division multiplexing

Received: October 11, 2023
Revised: November 19, 2023
Published online: December 7, 2023

[1] D. Amodei, D. Hernandez, AI and Compute, https://openai.com/research/ai-and-compute (accessed: September **2023**).
[2] *Nat. Electron.* **2023**, *6*, 329.
[3] B. J. Shastri, A. N. Tait, T. Ferreira De Lima, W. H. P. Pernice, H. Bhaskaran, C. D. Wright, P. R. Prucnal, *Nat. Photonics* **2021**, *15*, 102.
[4] C. Demirkiran, F. Eris, G. Wang, J. Elmhurst, N. Moore, N. C. Harris, A. Basumallik, V. J. Reddi, A. Joshi, D. Bunandar, *ACM J. Emerging Technol. Comput. Syst.* **2023**, *19*, 1.
[5] A. Sludds, S. Bandyopadhyay, Z. Chen, Z. Zhong, J. Cochrane, L. Bernstein, D. Bunandar, P. B. Dixon, S. A. Hamilton, M. Streshinsky, A. Novack, T. Baehr-Jones, M. Hochberg, M. Ghobadi, R. Hamerly, D. Englund, *Science* **2022**, *378*, 270.
[6] L. S. Madsen, F. Laudenbach, M. F. Askarani, F. Rortais, T. Vincent, J. F. F. Bulmer, F. M. Miatto, L. Neuhaus, L. G. Helt, M. J. Collins, A. E. Lita, T. Gerrits, S. W. Nam, V. D. Vaidya, M. Menotti, I. Dhand, Z. Vernon, N. Quesada, J. Lavoie, *Nature* **2022**, *606*, 75.
[7] M. Butcher, This startup hopes photonics will get us to AI systems faster, https://techcrunch.com/2022/05/12/this-startup-hopes-photonics-to-will-get-us-to-ai-systems-faster (accessed: September **2023**).
[8] PsiQuantum Will Partner with DARPA to Accelerate Path to Build the World's First Utility-Scale Quantum Computer, https://psiquantum.com/news/psiquantum-will-partner-with-darpa-to-accelerate-path-to-build-the-worlds-first-utility-scale-quantum-computer (accessed: September **2023**).
[9] Xanadu closes $100M USD Series C to accelerate development of fault-tolerant quantum computers, https://xanadu.ai/press/xanadu-closes-100M-USD-series-c-to-accelerate-development-of-fault-tolerant-quantum-computers (accessed: September **2023**).
[10] T. Weiland, Celestial AI, the Creator of the Photonic Fabric Optical Interconnect Technology Platform, Raises $100 Million in Series B Funding, https://www.businesswire.com/news/home/20230627995436/en/Celestial-AI-the-Creator-of-the-Photonic-Fabric-Optical-Interconnect-Technology-Platform-Raises-100-Million-in-Series-B-Funding (accessed: September **2023**).
[11] Y. Shen, N. C. Harris, S. Skirlo, M. Prabhu, T. Baehr-Jones, M. Hochberg, X. Sun, S. Zhao, H. Larochelle, D. Englund, M. Soljacic, *Nat. Photonics* **2017**, *11*, 441.
[12] J. Feldmann, N. Youngblood, M. Karpov, H. Gehring, X. Li, M. Stappers, M. Le Gallo, X. Fu, A. Lukashchuk, A. S. Raja, J. Liu, C. D. Wright, A. Sebastian, T. J. Kippenberg, W. H. P. Pernice, H. Bhaskaran, *Nature* **2021**, *589*, 52.
[13] L. Liao, S. Fathololoumi, K. Nguyen, H. Mahalingam, D. Hui, J. Heck, H. Frish, R. Defrees, C. Malouin, P. Seddighian, M. Huang, K. Al-hemyari, Y.-J. Chen, Y. Wang, W. Lin, D. Zhu, R. Jones, Y. Akulova, T. Liljeberg, in *Optical Fiber Communication Conf. (OFC) 2023*, Optica Publishing Group, San Diego, CA **2023**, p. Th3B.1.
[14] A. Rizzo, A. Novick, V. Gopal, B. Y. Kim, X. Ji, S. Daudlin, Y. Okawachi, Q. Cheng, M. Lipson, A. L. Gaeta, K. Bergman, *Nat. Photonics* **2023**, *17*, 781.
[15] C. Ríos, M. Stegmaier, P. Hosseini, D. Wang, T. Scherer, C. D. Wright, H. Bhaskaran, W. H. P. Pernice, *Nat. Photonics* **2015**, *9*, 725.

© 2023 The Authors. Advanced Materials published by Wiley-VCH GmbH

15214095, 2024, 8, Downloaded from https://onlinelibrary.wiley.com/doi/10.1002/adma.202310596 by University Of Exeter, Wiley Online Library on [19/06/2024]. See the Terms and Conditions (https://onlinelibrary.wiley.com/terms-and-conditions) on Wiley Online Library for rules of use; OA articles are governed by the applicable Creative Commons License

[16] C. Ríos, N. Youngblood, Z. Cheng, M. Le Gallo, W. H. P. Pernice, C. D. Wright, A. Sebastian, H. Bhaskaran, *Sci. Adv.* **2019**, *5*, eaau5759.
[17] R. Chen, Z. Fang, C. Perez, F. Miller, K. Kumari, A. Saxena, J. Zheng, S. J. Geiger, K. E. Goodson, A. Majumdar, *Nat. Commun.* **2023**, *14*, 3465.
[18] X. Xing, Y. Liu, J. Han, W. Liu, Z. Wei, *ACS Photonics* **2023**, *10*, 2264.
[19] M. Santandrea, M. Stefszky, V. Ansari, C. Silberhorn, *New J. Phys.* **2019**, *21*, 033038.
[20] A. Prinzen, M. Waldow, H. Kurz, *Opt. Express* **2013**, *21*, 17212.
[21] J. Pond, G. S. C. Lamant, R. Goldman, in *Optical Fiber Telecommunications VII* (Ed.: A. E. Willner), Academic Press, Cambridge, MA **2020**, pp. 195.
[22] M. Y.-S. Fang, S. Manipatruni, C. Wierzynski, A. Khosrowshahi, M. R. Deweese, *Opt. Express* **2019**, *27*, 14009.
[23] C. Levy, Z. Xuan, D. Huang, R. Kumar, J. Sharma, T. Kim, C. Ma, G.-L. Su, S. Liu, J. Kim, X. Wu, G. Balamurugan, H. Rong, J. Jaussi, in *2023 IEEE Custom Integrated Circuits Conf. (CICC)*, IEEE, Piscataway, NJ **2023**, pp. 1–2.
[24] A. Chakravarty, K. Schmidtke, V. Zeng, S. Giridharan, C. Deal, R. Niazmand, in *Frontiers in Optics 2017*, OSA, Washington, DC **2017**, paper JW4A.65.
[25] D. J. Blumenthal, H. Ballani, R. O. Behunin, J. E. Bowers, P. Costa, D. Lenoski, P. A. Morton, S. B. Papp, P. T. Rakich, *J. Lightwave Technol.* **2020**, *38*, 3376.
[26] W. Bogaerts, S. K. Selvaraja, P. Dumon, J. Brouckaert, K. De Vos, D. Van Thourhout, R. Baets, *IEEE J. Sel. Top. Quantum Electron.* **2010**, *16*, 33.
[27] K. Padmaraju, K. Bergman, *Nanophotonics* **2014**, *3*, 269.
[28] R. Soref, B. Bennett, *IEEE J. Quantum Electron.* **1987**, *23*, 123.
[29] S. Liu, J. Feng, Y. Tian, H. Zhao, L. Jin, B. Ouyang, J. Zhu, J. Guo, *Front. Optoelectron.* **2022**, *15*, 9.
[30] J. Schrauwen, D. Van Thourhout, R. Baets, *Opt. Express* **2008**, *16*, 3738.
[31] L. Thiel, A. D. Logan, S. Chakravarthi, S. Shree, K. Hestroffer, F. Hatami, K.-M. C. Fu, *Opt. Express* **2022**, *30*, 6921.
[32] N. Farmakidis, H. Yu, J. S. Lee, J. Feldmann, M. Wang, Y. He, S. Aggarwal, B. Dong, W. H. P. Pernice, H. Bhaskaran, *Nano Lett.* **2023**, *23*, 4800.
[33] M. M. Milosevic, X. Chen, W. Cao, A. F. J. Runge, Y. Franz, C. G. Littlejohns, S. Mailis, A. C. Peacock, D. J. Thomson, G. T. Reed, *IEEE J. Sel. Top. Quantum Electron.* **2018**, *24*, 1.
[34] H. Jayatilleka, H. Frish, R. Kumar, J. Heck, C. Ma, M. Sakib, D. Huang, H. Rong, *J. Lightwave Technol.* **2021**, *39*, 5083.
[35] S. M. Sze, *Semiconductor Devices: Physics and Technology*, John Wiley & Sons, Singapore **2012**.
[36] D. J. Moss, R. Morandotti, A. L. Gaeta, M. Lipson, *Nat. Photonics* **2013**, *7*, 597.
[37] W. Bogaerts, P. De Heyn, T. Van Vaerenbergh, K. De Vos, S. Kumar Selvaraja, T. Claes, P. Dumon, P. Bienstman, D. Van Thourhout, R. Baets, *Laser Photonics Rev.* **2012**, *6*, 47.
[38] A. Slawska-Waniewska, A. Siemko, G. Serfözö, *J. Magn. Magn. Mater.* **1991**, *93*, 169.
[39] K. P. Müller, J. Pelka, *Microelectron. Eng.* **1987**, *7*, 91.
[40] F. Brückerhoff-Plückelmann, J. Feldmann, H. Gehring, W. Zhou, C. D. Wright, H. Bhaskaran, W. Pernice, *Nanophotonics* **2022**, *11*, 4063.
[41] A. Rizzo, A. Novick, V. Gopal, B. Y. Kim, X. Ji, S. Daudlin, Y. Okawachi, Q. Cheng, M. Lipson, A. L. Gaeta, K. Bergman, *Nat. Photonics* **2023**, *17*, 781.
[42] A. Fawzi, M. Balog, A. Huang, T. Hubert, B. Romera-Paredes, M. Barekatain, A. Novikov, F. J. R. Ruiz, J. Schrittwieser, G. Swirszcz, D. Silver, D. Hassabis, P. Kohli, *Nature* **2022**, *610*, 47.
[43] N. P. Jouppi, C. Young, N. Patil, D. Patterson, G. Agrawal, R. Bajwa, S. Bates, S. Bhatia, N. Boden, A. Borchers, R. Boyle, P. Cantin, C. Chao, C. Clark, J. Coriell, M. Daley, M. Dau, J. Dean, B. Gelb, T. V. Ghaemmaghami, R. Gottipati, W. Gulland, R. Hagmann, C. R. Ho, D. Hogberg, J. Hu, R. Hundt, D. Hurt, J. Ibarz, A. Jaffey, et al., in *Proc. of the 44th Annual Int. Symp. on Computer Architecture*, Association For Computing Machinery, New York, NY **2017**, pp. 1.
[44] J. Li, S.-G. Ren, Y. Li, L. Yang, Y. Yu, R. Ni, H. Zhou, H. Bao, Y. He, J. Chen, H. Jia, X. Miao, *Sci. Adv.* **2023**, *9*, eadf7474.
[45] S. Bandyopadhyay, A. Sludds, S. Krastanov, R. Hamerly, N. Harris, D. Bunandar, M. Streshinsky, M. Hochberg, D. Englund, *arXiv:2208.01623* **2022**.
[46] C. Huang, S. Fujisawa, T. F. De Lima, A. N. Tait, E. C. Blow, Y. Tian, S. Bilodeau, A. Jha, F. Yaman, H.-T. Peng, H. G. Batshon, B. J. Shastri, Y. Inada, T. Wang, P. R. Prucnal, *Nat. Electron.* **2021**, *4*, 837.
[47] F. Ashtiani, A. J. Geers, F. Aflatouni, *Nature* **2022**, *606*, 501.
[48] J. Wang, S. P. Rodrigues, E. M. Dede, S. Fan, *Opt. Express* **2023**, *31*, 18871.
[49] H. Gehring, M. Blaicher, W. Hartmann, W. H. P. Pernice, *OSA Continuum* **2019**, *2*, 3091.
[50] FIB-SEM for FIB-centric nanofabrication, https://raith.com/product/velion/ (accessed: September **2023**).
[51] B. Tatian, *Appl. Opt.* **1984**, *23*, 4477.
[52] K. Luke, Y. Okawachi, M. R. E. Lamont, A. L. Gaeta, M. Lipson, *Opt. Lett.* **2015**, *40*, 4823.

© 2023 The Authors. Advanced Materials published by Wiley-VCH GmbH

15214095, 2024, 8, Downloaded from https://onlinelibrary.wiley.com/doi/10.1002/adma.202310596 by University Of Exeter, Wiley Online Library on [19/06/2024]. See the Terms and Conditions (https://onlinelibrary.wiley.com/terms-and-conditions) on Wiley Online Library for rules of use; OA articles are governed by the applicable Creative Commons License